

# Frequency and Voltage Compliance Capabilities of Grid-Forming Wind Turbines in Offshore Wind Farms in Weak AC Grids †

**Vilmann, Benjamin; Randewijk, Peter Jan; Jóhannsson, Hjörtur; Hjerrild, Jesper; Khalil, Ashraf**

*Published in:*
Electronics

*Link to article, DOI:*
10.3390/electronics12051114

*Publication date:*
2023

*Document Version*
Publisher's PDF, also known as Version of record

*electronics*

MDPI

*Article*

# Frequency and Voltage Compliance Capabilities of Grid-Forming Wind Turbines in Offshore Wind Farms in Weak AC Grids †

**Benjamin Vilmann [1,2,*], Peter Jan Randewijk [3], Hjörtur Jóhannsson [1], Jesper Hjerrild [2] and Ashraf Khalil [4]**

[1] Department of Wind and Energy Systems, Technical University of Denmark, 2800 Kongens Lyngby, Denmark
[2] Ørsted Wind Power A/S, 7000 Fredericia, Denmark
[3] Energinet Systemansvar A/S, 7000 Fredericia, Denmark
[4] DTU Engineering Technology, Technical University of Denmark, 2750 Ballerup, Denmark
* Correspondence: benvi@orsted.com
† This paper is an extended version of our paper published in UPEC.

**Abstract:** Weak grid conditions challenge the grid integration of offshore wind farms. Especially grids with low inertia and large grid impedance questions frequency and voltage compliance capabilities. Grid-forming wind turbines are a promising technology for weak grids due to the nature of their control strategy. This paper explains the difference in how weak grid conditions are described in the literature and shows how the voltage stability margin changes with the short-circuit ratio and X/R ratio. With that knowledge, the frequency and voltage compliance capabilities of three grid-forming controls in an offshore wind farm are investigated and benchmarked. These three controls are a droop control, a virtual synchronous machine, and a synchronverter. This was done by quantifying their performance during a frequency disturbance with sensitivity to the short-circuit ratio, X/R ratio, and the inertia constant, H. It is concluded that the virtual synchronous machine is the most compliant grid-forming control and that DC-link modeling is of great importance when testing compliance during frequency disturbances.

**Keywords:** frequency stability; grid-forming; weak grid; voltage stability; droop control; PV-curves; synchronverter; virtual synchronous machine; offshore wind farm



**Citation:** Vilmann, B.; Randewijk, P.J.; Jóhannsson, H.; Hjerrild, J.; Khalil, A. Frequency and Voltage Compliance Capabilities of Grid-Forming Wind Turbines in Offshore Wind Farms in Weak AC Grids. *Electronics* **2023**, *12*, 1114. https://doi.org/10.3390/electronics12051114

Academic Editors: Oguzhan Ceylan, Murat Gol and Aydogan Ozdemir

Received: 31 January 2023
Revised: 13 February 2023
Accepted: 20 February 2023
Published: 24 February 2023



## 1. Introduction

The penetration rate of wind energy has increased in the last two decades [1]. However, the introduction of more wind power from potent wind energy sites (PWESs) into power systems is challenged by several factors: (I) PWESs are often far away from the site of consumption, and the large impedance at the point of interconnection (POI) due to the long transmission lines is known as a weak AC grid connection point. Such connection points are related to volatile voltage transient responses [2]. (II) By replacing the power generation from synchronous generators (SGs) with offshore wind farms (OWFs), the inherent stability properties of SGs in terms of damping torque and inertia are somewhat lost or reduced [3,4]. A grid-following (GFL) control strategy for wind turbines (WTs) has been dominating the industry, but the grid-forming (GFM) control strategy is now gaining attention because it introduces some of the stability properties of an SG into converter-based power generation. The main motivation of this paper is, thus, to investigate how an OWF implemented with GFM control performs in terms of frequency and voltage compliance.. Note that this paper is an extension of a conference paper presented at the Universities Power Engineering Conference (UPEC) 2022 [5].

The definition of a weak grid is ambiguous and requires some elaboration. When the first OWFs were built in the 1990s, a weak grid referred to a volatile grid voltage [6]. Today, grids are classified as weak if the voltage and angle are sensitive to changes in the

current injection [7]. This sensitivity is usually classified according to the short-circuit ratio (SCR) [2,8]. The SCR is the ratio between the initial symmetric short-circuit power of the grid and the short-circuit power of the infeed [9]. However, because OWFs are often far away from synchronous generators (SGs), the initial symmetric short-circuit contribution from the SGs is neglected, as indicated by IEC 60909 [10]. As the sub-transient reactance of SGs is often around 0.2 pu [11], the initial short-circuit contribution is five times larger than the steady-state short-circuit current [12]. The difference in the resulting short-circuit power is huge and the effect has not been elaborated upon in the literature considered in this study. Many papers proposed that the short-circuit ratio (SCR) is fundamental for system strength classification [3,6,13–17] (these are elaborated upon later in Section 2.1), but there is disagreement about the SCR values distinguishing weak grids from strong ones. This might be due to the unclear short-circuit contributions from SGs, but it is not evident. That being said, there are other formulations of the SCR as a grid strength classification parameter accounting for neighboring inverter-based resources in various ways, which will not be covered in this paper [3,18].

Furthermore, the SCR is a fictitious value, as it is determined by the product of the initial symmetrical short-circuit current $i''_{sc}$, the nominal system voltage $V_{nom}$, and the factor $\sqrt{3}$ [10]. This implies that the impedance specifications, such as the reactance–resistance ratio $X/R$, are neglected in most cases—even though they impact the transient current limitation, the damping [19], and the active power transfer capabilities [20]. A few studies have included the $X/R$ ratio [21,22] in their investigations. Parts of the WT manufacturing industry acknowledge that the SCR cannot reflect all grid parameters as well, and they have proposed a complete WT control solution based on the analysis of the relations of $\delta P/\delta\theta$ and $\delta Q/\delta V$ [23]The $X/R$ is fundamental for this analysis.

Low-inertial-power systems have also been addressed as a problem in weak grids [3]. This is due to the low inertia and weak damping, which easily cause undesired oscillations in the system through grid dynamics [24]. There is a clear correlation between more converter-based power generation and lower system inertia [25]. This means that the frequency control from the converter-based generation must be sufficient for a successful implementation of renewable energy sources in a power system. The operational system frequency is required to be to be within a small band from the nominal frequency by the transmission system operators (TSOs), as some components are sensitive to frequency deviations and are linked to protective requirements. The following examples serve to provide an idea of the numbers and variety of grid code requirements. The Danish TSO, Energinet, requires the protection of wind power plants to withstand a rate-of-change-of-frequency (ROCOF) of $\pm$2.5 Hz/s and to stay online in system frequencies between 47 and 52 Hz [26]. The TSO in Great Britain, the National Grid, requires an operation frequency on a system level within $\pm$0.2 Hz and an ROCOF protection to withstand $\pm$0.125 Hz/s [27,28]. Many events can cause a frequency disturbance directly or indirectly. Examples are a sudden change in demand, generators failing, critical lines tripping, or area separations (islanding). Cases of such incidents cover, among other things, sub-synchronous small-signal stability issues that cause converters to malfunction and black-outs to emerge through a cascade of events ($f_{min} = 48.8$ Hz, $|ROCOF|_{max} > 0.125$ Hz/s) [28], as well as area separation in the continental power system ($f_{max} = 50.6$ Hz, $|ROCOF|_{max} = 0.3$ Hz/s) [29,30].

The main problem with weak grid classification is that it depends on the impedance magnitude, impedance angle, and the inertia, but no clear methodology has been devised for a mix of these three parameters. CIGRE is the only source found [3] that defined weak grid thresholds for the SCR, the $X/R$ ratio, and the inertia in the same document, but without relating them for classification purposes. It is the motivation of this paper to investigate frequency and voltage compliance capabilities in terms of the SCR, $X/R$, and inertia.

The traditional control of WTs is based on a GFL technique, where a phase-locked loop (PLL) is absolutely necessary. The presence of a PLL reduces the stability margin [31,32] and might lead to synchronization instabilities [33]. It is, thus, obvious that the stability margin of GFL wind turbines operating in weak grid conditions is further minimized. In [34], a relatively slow PLL was identified to be more prone to instability issues than a faster one. In [35], the critical point for inverter–grid voltage stability was described with respect to a minimum SCR regarding small-signal stability.

GFM WTs are a promising new solution for OWF applications, as they do not depend on a reference voltage for the PLL [36]. Papers emerged in 2009 and 2011 with options for the current loop of the converter to mimic a synchronous machine by using a virtual impedance. The pioneering formulations of the GFM control are known as the virtual synchronous machine (VSM) [37,38] and the synchronverter (SV) [39]. Other GFM control strategies, such as droop control, have emerged since then, and elaborate reviews on these GFM control strategies are available [31,40]. This paper will not go into detail with other control strategies, as they are outside the scope of the study. Only the control strategies listed in Table 1 will be investigated.

**Table 1.** GFM control strategies considered in this study.

| **Control Strategy** | | **Sources** |
|---|---|---|
| Droop control | (D) | [41] |
| Virtual synchronous machine | (VSM) | [42,43] |
| Synchronverter | (SV) | [39] |

The choice of these is relevant due to their wide acceptance and applicability. Droop control is simple and well known. The VSM has been used in some pilot projects [44] and has been the framework for grid codes and grid-forming capabilities for the National Grid [45]. The SV was studied for comparative purposes with respect to another "virtual synchronous machine" regarding inertia emulation.

The choice of these GFM control strategies was further backed by the availability of templates in DIgSILENT's PowerFactory (PF, version 2021 SP4), i.e. pre-designed implementations of the GFM control strategies. Because the focus of this paper is grid-converter dynamics in weak grid conditions and not the optimization of tuning parameters, no further changes to the templates are made. The tuning parameters are found in Table A1

The main contributions of this paper are, thus, *(a)* an extensive sensitivity analysis of the SCR, $X/R$ ratio, and inertia constant $H$, *(b)* a proof of concept of an OWF with GFM control serving as the main frequency support in some weak grids, and *(c)* the highlighting of DC-link modeling as inevitable for studies of GFM controls subjected to frequency disturbances.

This paper is organized as follows: Section 2 sketches the discrepancies in the common definition of a weak grid in the literature. Section 3 explains the dependence of the voltage on the power flow across a line and the impacts of the impedance magnitude and phase. This is the context in which the GFM controls are explained in Section 4. Section 5 elaborates on the case study's configuration and the model used. Section 6 presents the results. Sections 7 and 8 evaluate and conclude on the benchmarking results, respectively.

## 2. Weak Grid Definition

Weak grids are considered as high-impedance connection points and have a volatile voltage. Thus, the short-circuit ratio (SCR) and the $X/R$ ratio are central concepts for grid strength classification. The inertia of the system also plays a role in voltage stability, as low-inertial systems require large changes in the power flow during power imbalances.

### *2.1. Short-Circuit Ratio (SCR)*

The SCR is defined as the short-circuit power level from the grid divided by the nominal infeed capacity, which is the OWF in this application:

$$SCR = \frac{s''_{sc}}{S_{nom,infeed}} \tag{1}$$

It is, thus, noted that the SCR is a local parameter and is considered at the point of interconnection (POI). There is a large discrepancy in the grid strength for defining SCR levels in the literature, as summarized in Table 2.

**Table 2.** Grid strength for defining SCR levels.

| Source | Very Weak | Weak | Strong |
|---|---|---|---|
| [6] | N.A. | < 10 | >20 |
| [3] | <3 | 3 < SCR < 5 | N.A. |
| [13] | <2 | 2 < SCR < 3 | >3 |
| [14] | N.A. | < 6–10 | >20–25 |
| [15] | 1 | N.A. | N.A. |
| [16] | N.A. | 6 | N.A. |

The initial short-circuit power, $s''_{sc}$, is a fictitious value [10] and does not consider the $X/R$ ratio of the impedance, but only the magnitude. The initial short-circuit current, $I''_{sc} \propto s''_{sc}$, differs from the short-circuit peak current, which considers the $X/R$ ratio, as seen in Figure 1. The SCR is, thus, an ambiguous grid-strength-defining parameter alone, as lower $X/R$ ratio values limit the current flow.

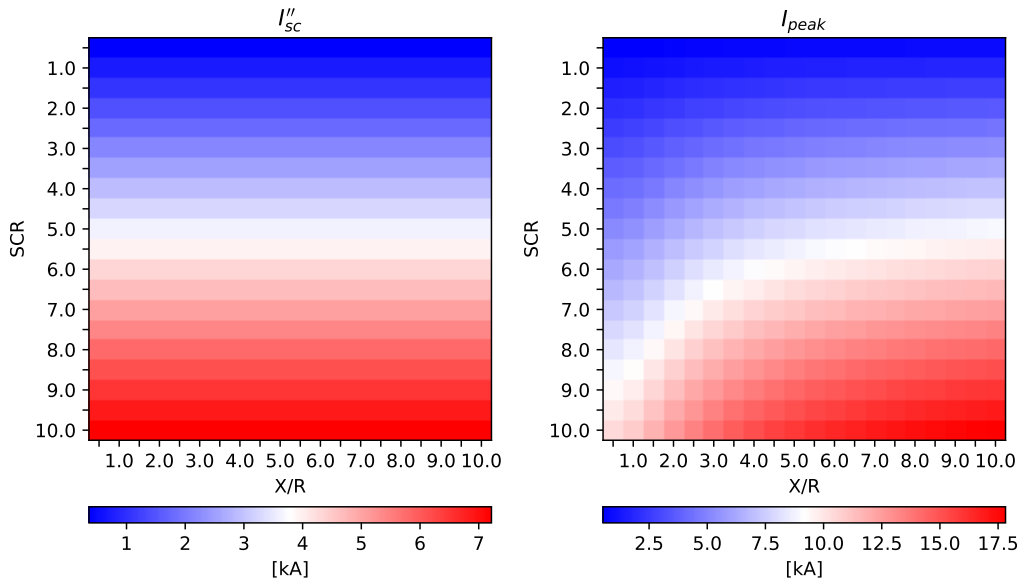


**Figure 1.** Short-circuit currents for various short-circuit ratios (SCR) and $X/R$ ratios from a three-phase fault. Note that the initial symmetric short-circuit current is given by $I''_{sc} = S''_{sc}/(\sqrt{3}V_{nom})$ and the peak short-circuit current is given by $I_{peak} = \kappa\sqrt{2}I''_{sc}$. Note that the scalar $\kappa$ is a function of $X/R$, such that: $\kappa = 1.02 + 0.98e^{-3R/X}$ [10].

### *2.2. X/R Ratio*

Ignoring sub-transient reactance from the grid, which is fair for far-from-generator locations, the grid impedance is defined as:

$$Z_g = \frac{V_g^2}{S_g} = \frac{V_g^2}{S_{nom,OWF} \cdot SCR} \tag{2}$$

The resistance and reactance are found by noting that the impedance angle is given by $\theta = \arctan(X/R)$:

$$\begin{aligned} R_g &= Z_g \cdot \cos\theta \\ X_g &= Z_g \cdot \sin\theta \end{aligned} \tag{3}$$

A trigonometric relation of the $X/R$ ratio is noted, and this explains the development of the limited short-circuit peak current shown in Figure 1. The $X/R$ ratio is a less-debated grid strength parameter in academia, but it plays a subtle role in terms of damping. In [3], an $X/R$ ratio below 3 was considered to indicate weak grid conditions, whereas an $X/R$ ratio of between 1 and 5 was defined as a low $X/R$ ratio. The $X/R$ ratio is also a local parameter, as it depends on the Thevenin equivalent of the grid impedance.

### *2.3. Inertia Constant H*

The inertia constant expresses the acceleration time constant of the system, $H = \tau_a/2$, and is a global parameter, unlike the SCR and the $X/R$ ratio. CIGRE provided indirectly grid-strength-defining inertia levels [3]. The relative inertia constant $H_i$ of the $i$th machine indicates the total kinetic energy $E_{kin,tot}$ of the system with respect to the $N$ online generators as a linear combination. This further relates to the absolute moment of inertia $J$ and the rotor frequency $\omega_r$:

$$E_{kin,tot} = \sum_i^N H_i S_{i,rat} = \sum_i^N \frac{1}{2} J_i \omega_r^2 \tag{4}$$

where $S_{i,rat}$ is the $i$th machine's rating. It is known that the ROCOF was derived from the swing equation [46]:

$$\frac{\mathrm{d}f}{\mathrm{d}t} = f_{nom} \frac{\Delta P}{2H} \tag{5}$$

The greater the inertia is, the lower the ROCOF realized from a power imbalance of a magnitude $\Delta P$ will be. Because the ROCOF depends on the power imbalance, as shown in (5), the grid strength from the inertia depends on the event parameter $\Delta P$. According to [3], the grid is considered weak if the ROCOF is greater than 1 and very weak if it is greater than 2. The event parameter $\Delta P$ is fixed in this study to 5% of the nominal OWF capacity. It is acknowledged that frequency compliance has many aspects in terms of duration. This study will only consider the immediate dynamic frequency response period (primary frequency response). In this context, it is worth noting that the frequency regulation services of OWFs must be aligned with dynamic wind forecasts.

## 3. Power Flow Changes and Voltage Stability Margin

The grid impedance magnitude and impedance angle impact the maximum power transfer capabilities of a line [20,47]. Any frequency recovery from a power imbalance in a grid caused by OWFs thus heavily relies on their voltage compliance capabilities and voltage stability margin. To elaborate on this sensitivity with respect to the SCR and the $X/R$ ratio, PV curves and PQV surface plots will be presented in this section. Note that the inertia constant parameter is omitted from this analysis, as it only affects the transient behavior.

The formal analysis is based on a simplified transmission line that depends on the voltage magnitude and angle of the sending and receiving ends, as illustrated in Figure 2.

This network is comparable to an OWF generating power for the grid, which is seen as a load, as illustrated in Figure 2b. The total complex power is considered:

$$I = \frac{V_s \angle(\delta - \theta)}{Z_{LN} \angle \phi + Z_{LD} \angle \theta} \tag{6}$$

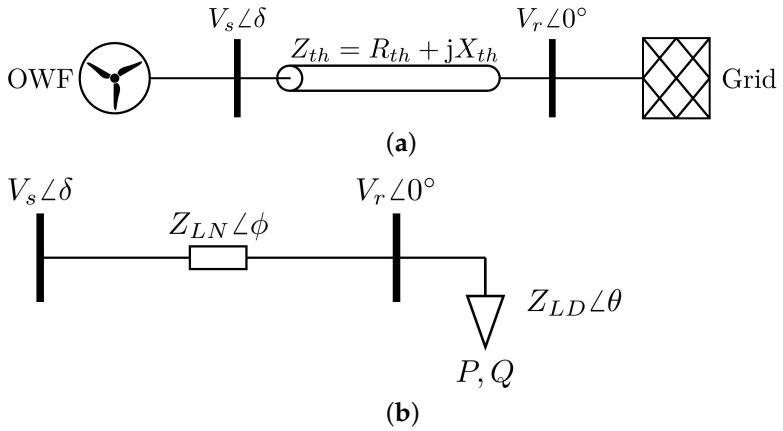


**Figure 2.** Network equivalents of an aggregated OWF for the PQV analysis. (**a**) Simplified single-line diagram of a transmission network of an OWF connected to the grid via a Thevenin impedance of the OWF. (**b**) Essential network equivalents for the network analysis.

It is possible to eliminate the dependency of the angles in the above expression via a network analysis [48,49]. The rewritten equation only depends on the magnitudes of the sending and receiving ends' voltages, the active and reactive power flow, and the resistance and reactance of the line ($V_s, V_r, P, Q, R, X$, respectively):

$$V_r^4 + V_r^2\left(2(RP + XQ) - V_s^2\right) + \left(R^2 + X^2\right)\left(P^2 + Q^2\right) = 0 \tag{7}$$

This equation yields two solutions for the active and reactive power and four solutions for voltage. It is noticed that the feasible solution space $\mathcal{F}$ only obtains voltages, resistances, and reactances equal to or greater than zero for physical consistency, i.e., $V_s, V_r, R, X \in \mathbb{R}^+$. It is noted that the feasible solution space $\mathcal{F}$ is a subset of the total solution space $\mathcal{S}$, such that $\mathcal{F} \subset \mathcal{S}$.

### *3.1. PV Curves, Power Factor, and Weak Grid Sensitivity*

PV curves are established by solving for the voltage in (7) with respect to a range of active power set points. The reactive power is evaluated at $Q = P\tan(\theta)$. The rest of the system values are set to somewhat arbitrary values for illustrative purposes at this point (i.e., $V_s = 132$ kV, $X = 100\ \Omega$, and $R = 0\ \Omega$). In Figure 3, various PV curves are plotted for different power factors.

The locus of critical points shows the respective point of voltage instability [50]. Any equilibrium point achieved below this point would affect the passive instability through other factors in the power system, e.g., tap-changers [51] and, thus, result in a voltage collapse. The effect of injecting reactive power into the system shows that voltage support also increases the voltage stability margin. The voltage stability margin refers to two relations in this context: (1) the margin from the point of operation to the tip of the PV curve and (2) the voltage deviation due to the change in active power. It is clear from the figure that $\theta = -10°$ is more robust to changes in the active power flow than $\theta = 0°$, and that the former yields the largest margin with respect to the critical point.

When considering the influence of weak grid parameters on the means of a large and fairly resistive Thevenin equivalent, the PV curves are drastically altered. In Figure 4, the PV curves are plotted for values of $SCR, X/R \in \{1, 5, 10\}$.

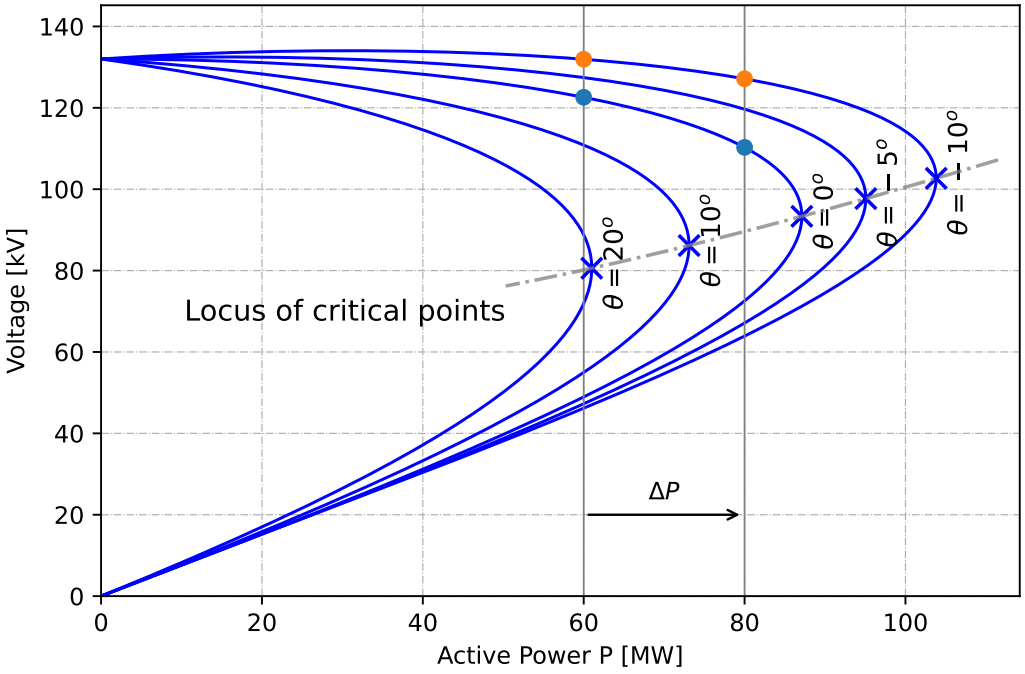


**Figure 3.** PV curves for multiple power factors.

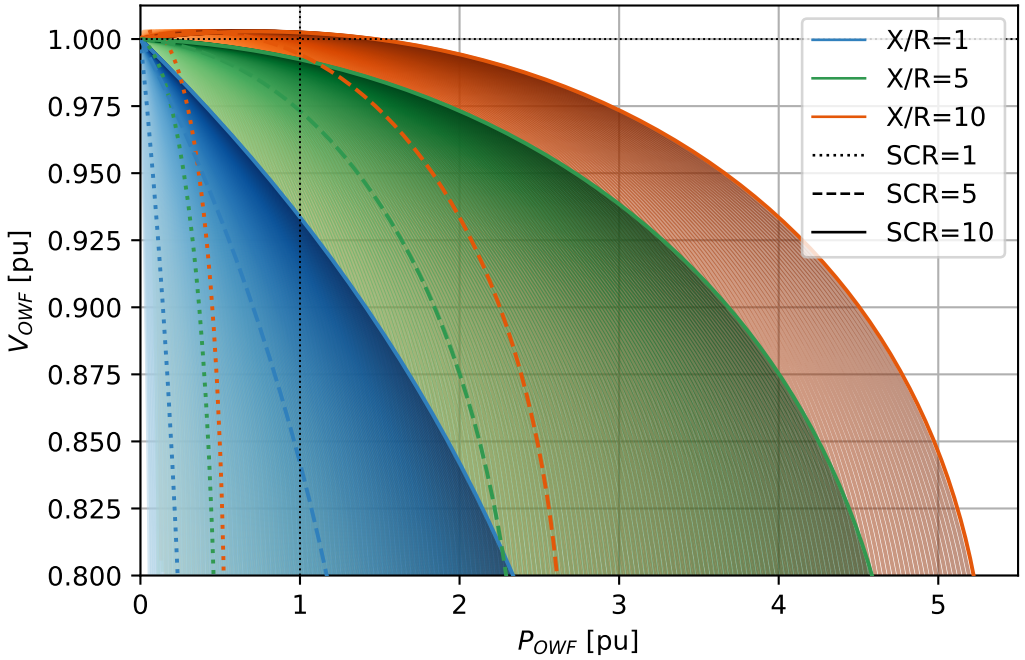


**Figure 4.** PV curves plotted for $SCR, X/R \in \{1, 5, 10\}$. The system is per-unitized, the voltage is only plotted to 0.8 pu, and there is no reactive power generation, i.e., power factor = 1. The colors distinguish the $X/R$ ratio; orange is the highest and blue the lowest. For each $X/R$ ratio plotted, there is a dotted, dashed, and solid line. The solidity of the line indicates the corresponding relative grid strength.

The colors distinguish the $X/R$ ratio; orange is the highest and blue the lowest. For each $X/R$ ratio plotted, there is a dotted, dashed, and solid line. The solidity of the line indicates the corresponding relative grid strength. In this manner, the orange solid line represents the PV curve of a strong grid, and the blue dotted line represents the PV curve of a weak grid ($SCR = X/R = 10$ and $SCR = X/R = 1$, respectively).

It is acknowledged that the SCR has a larger impact on the voltage stability margin seen at an operation point at $P = 1$ pu, and it is emphasized that a combination of weak grid conditions raises compliance concerns without any other grid-stabilizing equipment being considered. Acquiring flexible AC transmission system (FACTS) devices is costly [52] and would eventually challenge the techno-economic feasibility of an OWF project.

### *3.2. PQV Surface Plots and Voltage Stability Margin*

To better illustrate the impacts of the SCR and the $X/R$ ratio on the steady state from the feasible solution space $\mathcal{F}$ provided by (7) and the increased voltage stability margin obtained by injecting reactive power, the solution of the voltage from the equation was mapped into a PQ space. This resulted in the PQV surface plots in Figure 5, where $SCR, X/R \in \{3, 10\}$, and the PV curves are for $\theta \in \{0°, -10°, -20°\}$.

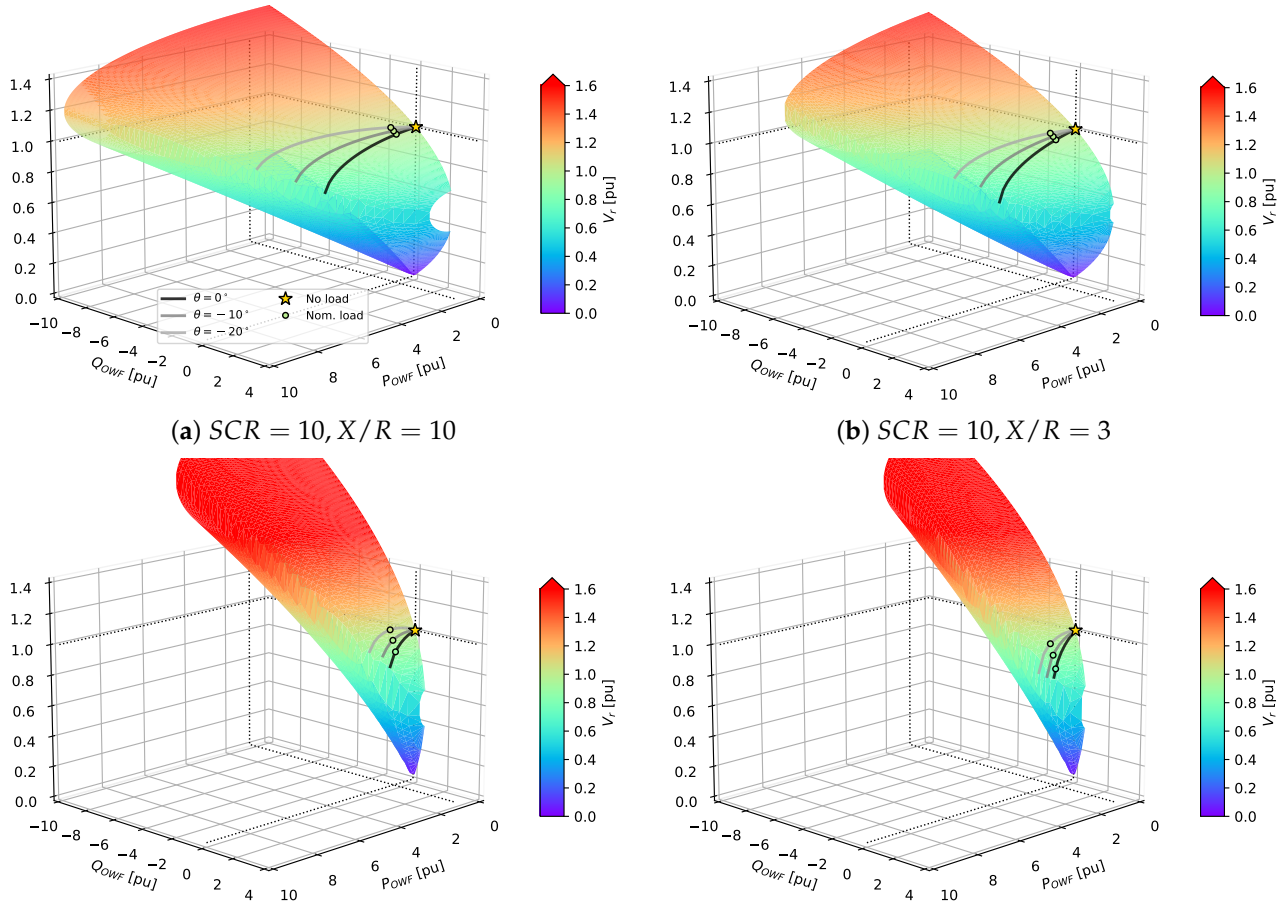


(**a**) $SCR = 10, X/R = 10$ (**b**) $SCR = 10, X/R = 3$

(**c**) $SCR = 3, X/R = 10$ (**d**) $SCR = 3, X/R = 3$

**Figure 5.** The feasible solution space $\mathcal{F}$ when expanding the PQV surfaces by solving (7). The 2D version is found in Figure 6.

Apart from the large volume into which the feasible solution space $\mathcal{F}$ expands, not much of the space is compliant with respect to the general grid code requirements and the PQ capabilities of an OWF by design. It is acknowledged that the compliant solution space $\mathcal{C} \subset \mathcal{F}$ is delimited by $V_{min}, V_{max}, Q_{min}, Q_{max}, P_{min}, P_{max}$.

The plots in Figure 5 illustrate that the compliant solution space is rather large for strong grids and quite small for weak grid conditions. In particular, the impedance magnitude limits the active power transfer capabilities, which, in strong grid conditions, exceeds the OWF's capacity by far. This provides good stability margins for the operation of the OWF.

The plots show that, for achieving compliant voltage levels, reactive power compensation is crucial for weak grids with low SCRs. However, if the $X/R$ ratio is also low, reactive power compensation loses its effect. This is explained by the increasing impact of coupling effects between resistance and reactance with respect to active power and reactive power (see [53]). This corresponds to the findings from Figure 4.

In Figure 6, the compliant solution space $\mathcal{C}$ of the voltage is shown by the blue–white–red gradient in the range of $[0.95; 1.05]$ pu. This is plotted on top of the feasible solution space $\mathcal{F}$, which is plotted with a gray-scale gradient.

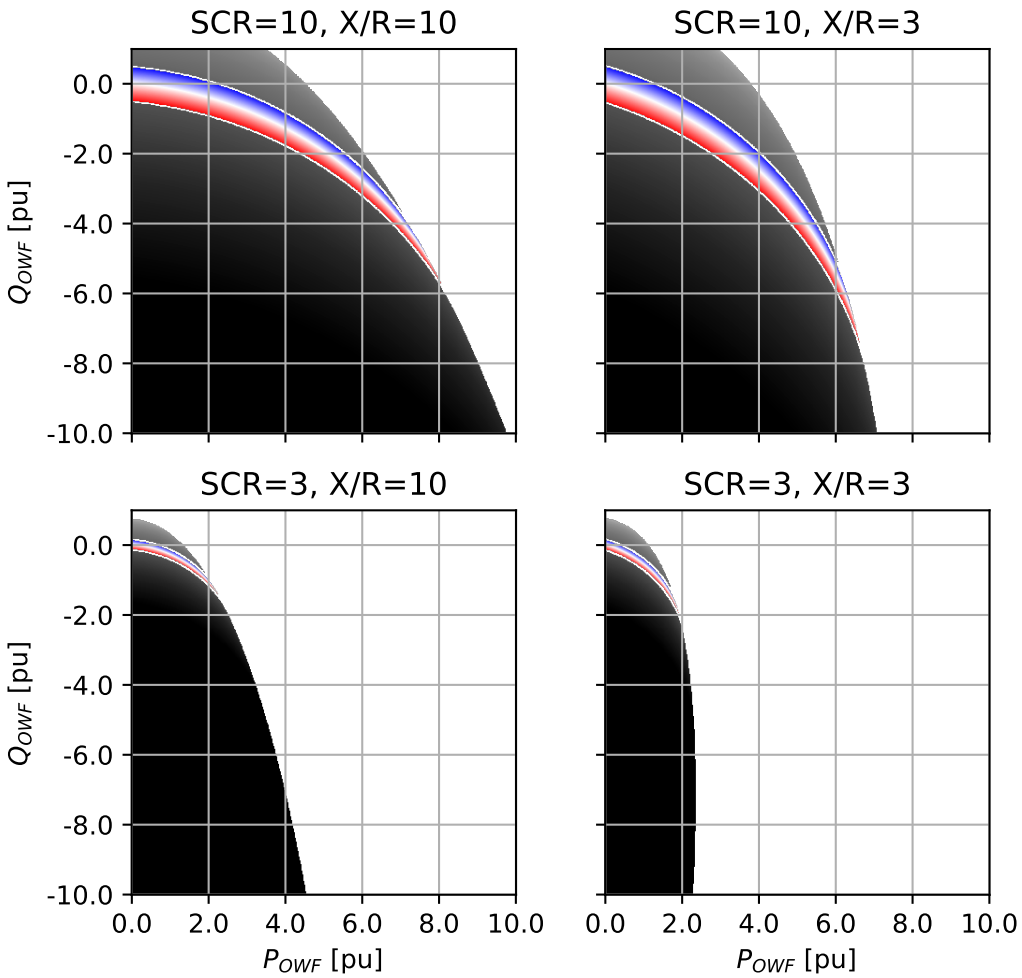


**Figure 6.** Compliant and feasible solution spaces ($\mathcal{C}$ and $\mathcal{F}$) of a transmission line seen in PQV space for $SCR, X/R \in \{3, 10\}$. The colors distinguish the $X/R$ ratio; orange is the highest and blue the lowest. For each $X/R$ ratio plotted, there is a dotted, dashed, and solid line. The solidity of the line indicates the corresponding relative grid strength. The plot is a 2D version of Figure 5.

The present PQV analysis is only valid for the steady state and ignores all dynamics of the system.

## 4. Grid-Forming Topologies

A well-established formulation of the concept of GFM converters is still under discussion [31]. However, a key difference between a GFL and a GFM converter is that they behave as a current source (CS) and a voltage source (VS), respectively. Even though both are voltage source inverters, they emulate this behavior with the control. Consider these converter topologies connected to the grid, as shown in Figure 7.

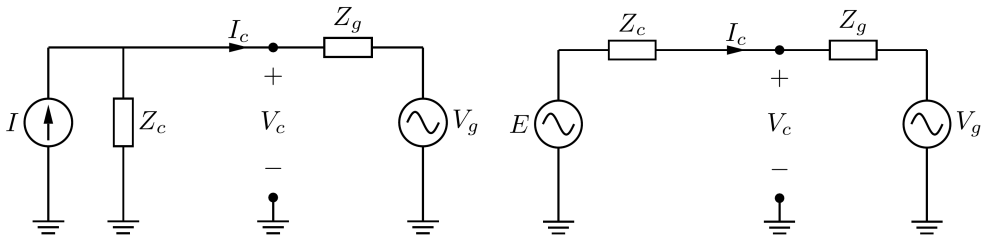


(**a**) Current source (CS) (**b**) Voltage source (VS)

**Figure 7.** Converter topologies (approximations).

By applying the KVL, the following can be derived:

$$\begin{aligned} &\text{CS:} \quad V_c = V_g + I_c \cdot (Z_g) \\ &\text{VS:} \quad V_c = E - I_c \cdot (Z_c) \end{aligned} \tag{8}$$

Thus, the GFM control adjusts the current to keep the virtual internal voltage, $E$, constant despite voltage perturbations. This is illustrated in Figure 8.

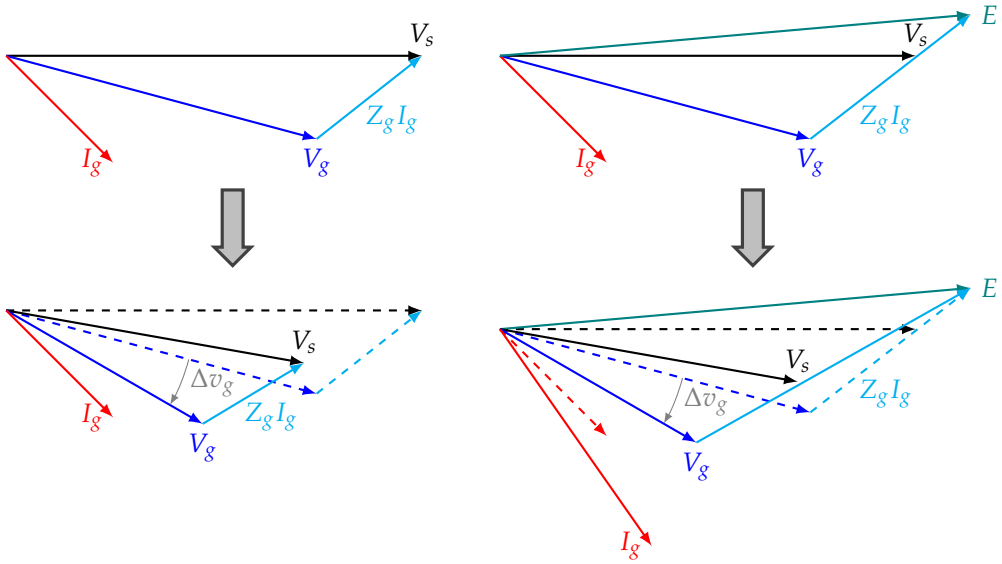


(**a**) GFL phasor diagram (**b**) GFM phasor diagram

**Figure 8.** Phasor relations of GFM and GFL converters due to grid voltage perturbations.

In this paper, three different control methods are investigated: droop control, the virtual synchronous machine (VSM), and the synchronverter.

### *4.1. Droop Control*

GFM droop control is achieved by implementing the droop equations:

$$f - f_{ref} = -m_p\left(P - P_{ref}\right) \tag{9}$$

$$V - V_{ref} = -m_q\left(Q - Q_{ref}\right) \tag{10}$$

where $f$ is the measured frequency, $f_{ref}$ is the frequency reference, $m_p$ is the active power droop gain, $P$ is the measured active power, $P_{ref}$ is the active power reference, $V$ is the measured voltage, $V_{ref}$ is the voltage reference, $m_q$ is the reactive power droop gain, $Q$ is the measured reactive power, and $Q_{ref}$ is the reactive power reference. These were implemented in PowerFactory, as seen in Figure A1 in Appendix A.

### *4.2. Virtual Synchronous Machine (VSM)*

The power synchronization loop of the VSM is created by implementing the swing equation while including damping. By rewriting the swing equation from (5) and recalling that $\tau_a = 2H$, the following can be derived:

$$\frac{\mathrm{d}}{\mathrm{d}t} f_{pu} = \frac{\Delta P}{\tau_a} = \frac{P_m - P_e - P_{friction}}{\tau_a} \tag{11}$$

where $\frac{\mathrm{d}f}{\mathrm{d}t}$ is the rate of change of frequency, $\Delta P$ is the power imbalance, $\tau_a$ is the acceleration constant, $P_m$ is the mechanical power, $P_e$ is the electrical power, and $P_{friction}$ is the damping loss. This was implemented as shown in Figure A2 in Appendix A.

### *4.3. Synchronverter (SV)*

The SV calculates the frequency and angle by considering the rotor motion (including the damping part). Power synchronization is performed by considering Newton's second law for an SG:

$$J\alpha(t) = T_m(t) - T_e(t) - D_p\omega_m(t) = T_a(t) \tag{12}$$

where $J$ is the inertia, $\alpha$ is the angular acceleration, $T_m$ is the mechanical torque, $T_e$ is the electrical torque, $D_p$ is the damping coefficient, $\omega_m$ is the mechanical angular velocity, and $T_a$ is the accelerating torque.

The model of the synchronverter was given in [39] and was implemented in PowerFactory, as shown in Figure A3 in Appendix A. The Zhong equations were implemented in PowerFactory (see also [54]) as follows:

$$\begin{aligned} &\text{Equation (7)} \quad T_e = M_f i_f \hat{i}\mathbf{cos}(\theta - \varphi) \\ &\text{Equation (8)} \quad e = \omega M_f i_f \mathbf{sin}(\theta) \\ &\text{Equation (9)} \quad P = \omega M_f i_f \hat{i}\mathbf{cos}(\theta - \varphi) \\ &\qquad\qquad\quad Q = \omega M_f i_f \hat{i}\mathbf{sin}(\theta - \varphi) \end{aligned} \tag{13}$$

where $M_f$ is the mutual virtual inductance, $i_f$ is the excitation current, $\hat{i}$ is the current amplitude, $\omega$ is the frequency, $\theta$ is the rotor angle, and $\varphi$ is the phase angle. The expressions in bold are vectors.

## 5. The Model of Offshore Wind Farm

A generic OWF design with 8 MW WTs are introduced of one cluster with six strings in the collector system as shown in Figure 9. Balanced RMS-simulations are performed to study frequency and voltage responses from a frequency disturbance from a power imbalance in the grid scaled to 5% of the installed OWF capacity. The grid voltage is modelled as a synchronous generator (SG) [12].

The power flow in the system of the base case while using the initial conditions for the frequency disturbance was considered, as shown in Figure 10.

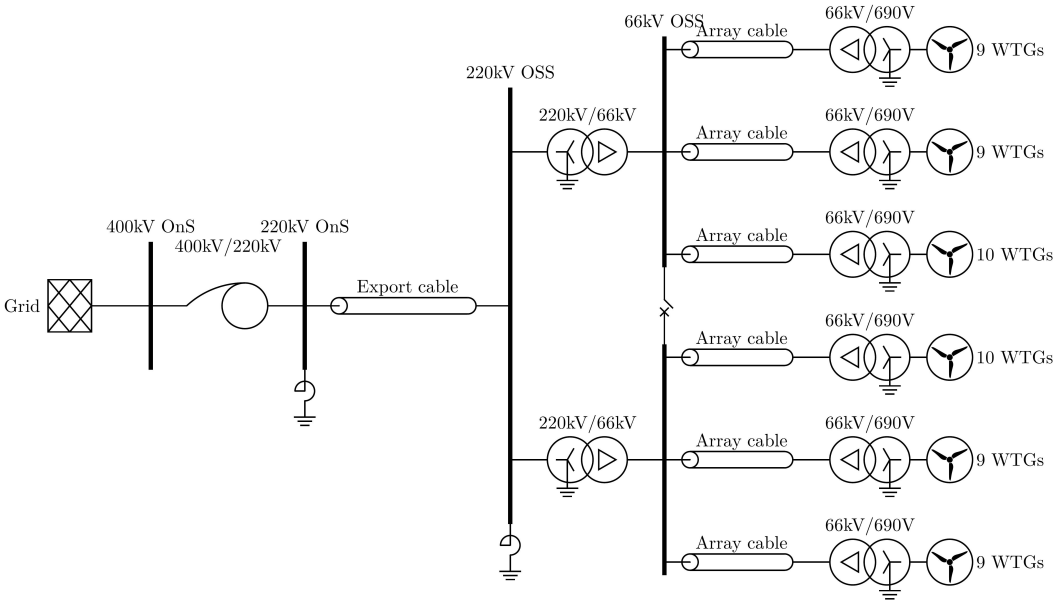


**Figure 9.** Generic offshore wind farm model.

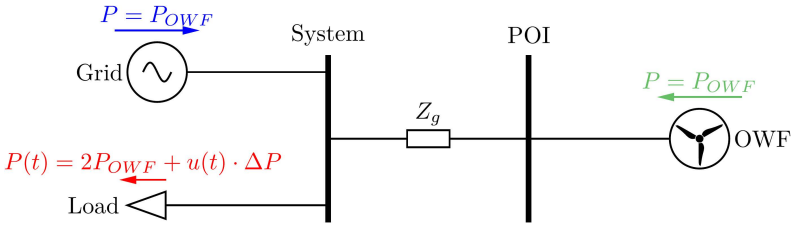


**Figure 10.** Aggregated power flow model.

To investigate the upward frequency regulation of the OWF, curtailed operation scenarios were also considered. The National Grid requires a minimum of 10% curtailment to enter balancing markets [55]. The test cases are defined in Table 3.

**Table 3.** Test case definitions.

| Test | | Generation and Demand [b] | | | Disturbance [b] |
|---|---|---|---|---|---|
| # | Op. [a] | Grid | OWF | Load | $\Delta P$ |
| **1** | C | 1.1 | 0.9 | $2 + \Delta P \cdot u(t)$ | 0.05 |
| **2** | C | 1.1 | 0.9 | $2 + \Delta P \cdot u(t)$ | $-0.05$ |
| **3** | N | 1.0 | 1.0 | $2 + \Delta P \cdot u(t)$ | $-0.05$ |

[a] Op. = Operation, C = Curtailed, N = Nominal. [b] All quantities are scaled to nominal capacity, $P_{OWF}$.

All simulations were performed in DIgSILENT's PowerFactory (version 2021, service package 4) while using the available GFM templates.

## 6. Results

### *6.1. Types of Responses*

The types of responses of the different GFM controls implemented in the OWF to a frequency disturbance under weak grid conditions are found in Figure 11.

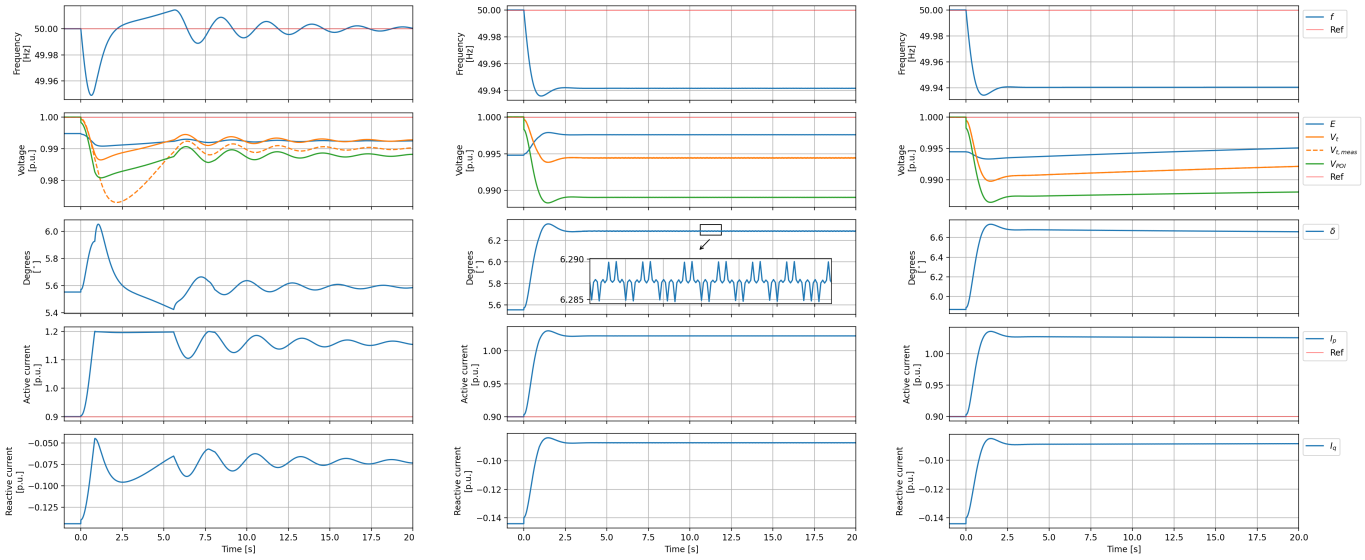


(**a**) Droop Control (**b**) Virtual Synchronous Machine (**c**) Synchronverter

**Figure 11.** Types of GFM responses for test case #1 (upward frequency regulation) for the following grid conditions: $SCR = 4, X/R = 2, H = 4$.

The droop control showed an aggressive and tightly tuned response. It was noticed that the droop coefficient was very small, as the frequency oscillated around the nominal value. Because the droop control compensated for the entire power imbalance, including accounting for the lost kinetic energy by accelerating the system again, it was noted that the active current was saturated by the converter's current limit at 1.2 pu. The imbalance was only equal to 0.05 pu, and the additional current losses were associated with the frequency and voltage.

The voltage angle $\delta$ did not follow a typical second-order system response, as it did for the VSM and SV. However, this was in accordance with the theory, since the latter two were derived from the swing equation, and the droop control was not.

The VSM and SV had a frequency disturbance response that would have been typical for a synchronous generator. This proved that the implementation and setup were correct. It was noticed that the voltage angle $\delta$ of the VSM suffered from an unstable limit cycle (as seen in Figure 11b). This was caused by various limiters in the control systems [56]. Furthermore, in [43], numerical issues with the VSM were also addressed. The responses of the VSM and SV looked very much alike, but the SV managed to restore the voltage because of the coupling between the inertial emulation and the voltage regulation via the Zhong equations, as seen in Figure 11c.

### *6.2. Trends of the SCR, X/R Ratio, and Inertia Constant H*

An automation script was implemented in Python, which allowed the parameters in PowerFactory to be swept. The SCR, $X/R$ ratio, and inertia constant $H$ were studied in the range of 1 to 10 in steps of 1 for the three GFM control topologies, and the three test cases are given in Table 3. This gave a total of 9000 dynamic simulations. To document the frequency and voltage compliance capabilities, it was desired to extract certain parameters. The benchmark parameters are given in Table 4.

**Table 4.** Impacts of the compliance parameters.

| *Benchmark Parameter* | | | *Impact Level* [b] | | | *Data Manipulation* | |
|---|---|---|---|---|---|---|---|
| **Symbol** | **Unit** | **Type** [a] | **SCR** | **X/R** | **H** | **Dim.** [c] | **P < W < F** [d] |
| $\frac{df}{dt}$ | Hz/s | P | H | L | H | X/R | 0 < 1 < 2 |
| $\Delta f$ | Hz | C | H | L | H | X/R | 0 < 0.5 < 2 |
| $f_{post,ss}$ | Hz | C | L | M | - | H | 0 < 0.5 < 2 |
| $\frac{dv}{dt}$ | p.u./s | P | H | L | H | X/R | 0 < 0.2 < 0.4 |
| $\Delta v$ | p.u. | C | H | L | H | X/R | 0 < 0.02 < 0.05 |
| $v_{post,ss}$ | p.u. | C | H | L | - | X/R | 0 < 0.02 < 0.05 |
| $\Delta E_{kin}$ | kWh | P | L | M | - | H | 0 < 10 < 20 |

[a] P = Performance, C = Compliance, [b] H = High, M = Medium, L = Low, [c] Reduced dimension, [d] P = Pass, W = Warn, F = Fail.

Some benchmark parameters were directly related to grid codes and provided qualification thresholds. Other parameters could be considered as performance indicators, and pass/fail thresholds were tentatively derived. Each benchmark parameter in the simulation results could be stored in a three-dimensional array for each test case and GFM scheme, as shown in Figure 12.

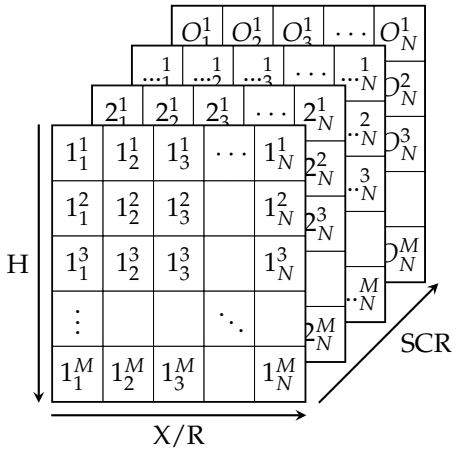


**Figure 12.** Matrix indices from sweeping SCR, X/R, and H.

To evaluate the performance, the arrays were reduced to two-dimensional heatmaps. The values were given by the maximum value in the dimension of the lowest-impact sweeping parameter (i.e., the SCR, $X/R$ ratio, or $H$). The impact level was based on the analysis of the sensitivity for test case #1 given in Figure 13. The performance evaluation is found in Figure 14

The analysis of the voltage and frequency trends with respect to the SCR, $X/R$ ratio, and $H$ was carried out by investigating the responses in Figure 13 for a range of fixed values, which are listed in Table 5.

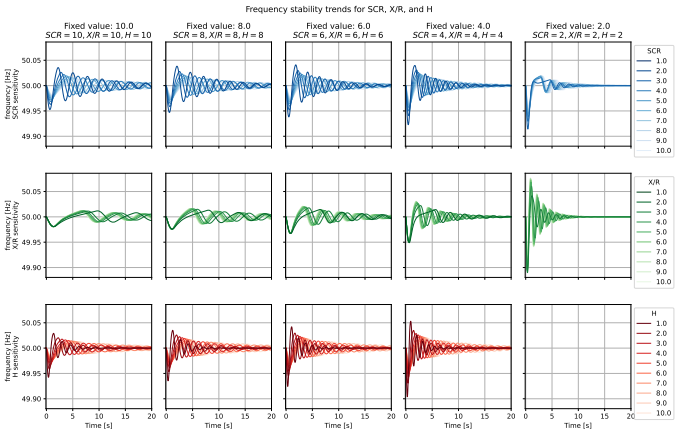


(**a**) Frequency (droop control)

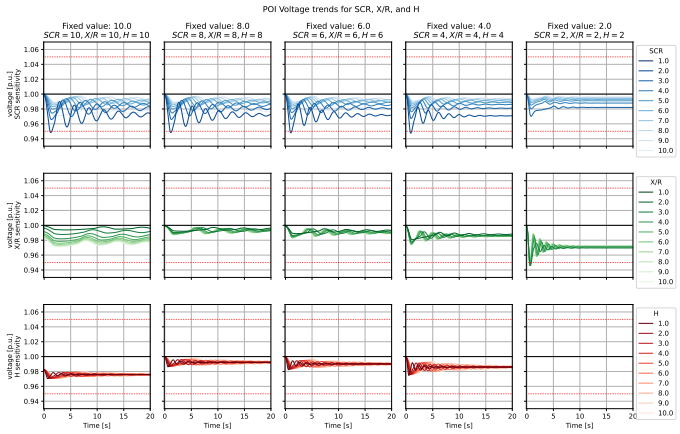


(**b**) Voltage (droop control)

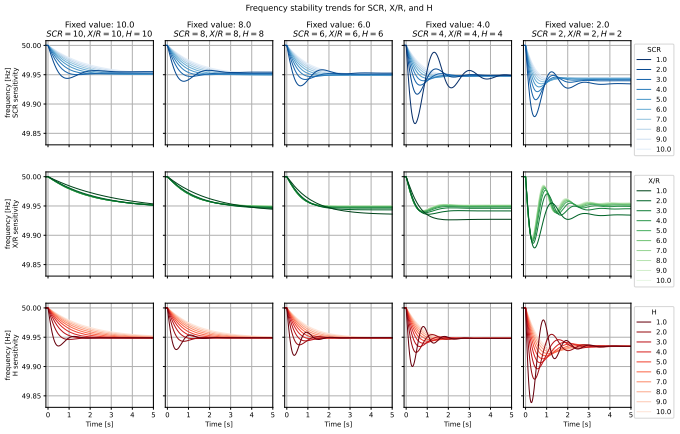


(**c**) Frequency (VSM)

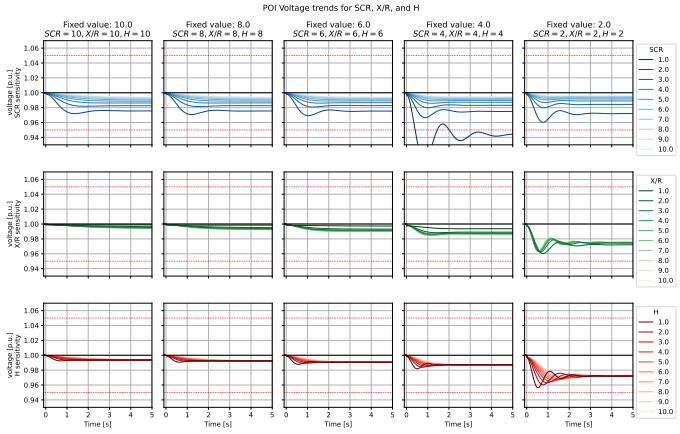


(**d**) Voltage (VSM)

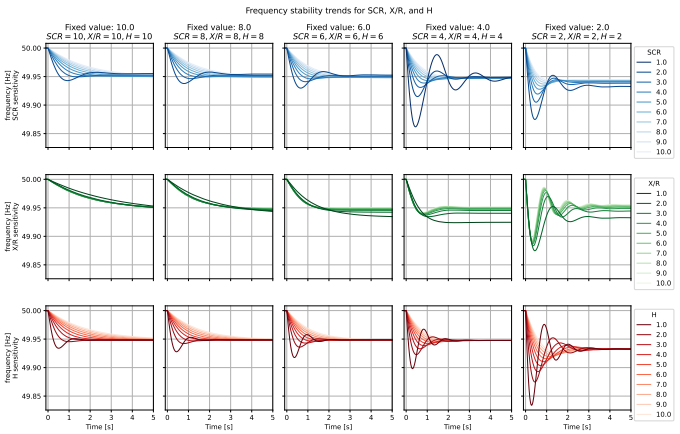


(**e**) Frequency (SV)

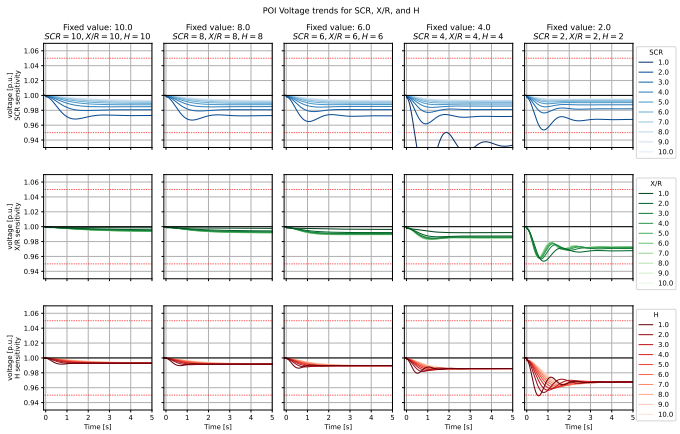


(**f**) Voltage (SV)

**Figure 13.** Preview of the trend plots (test case #1).

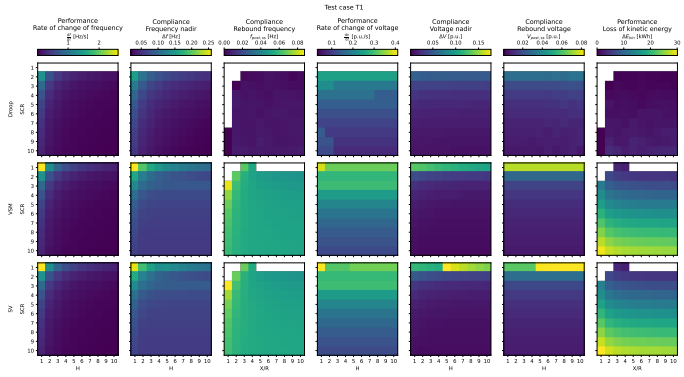

(**a**) Real values (Test #1)

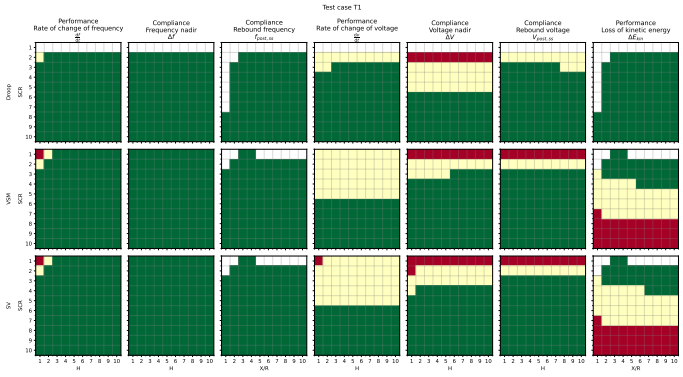

(**b**) Pass/fail mapping (Test #1)

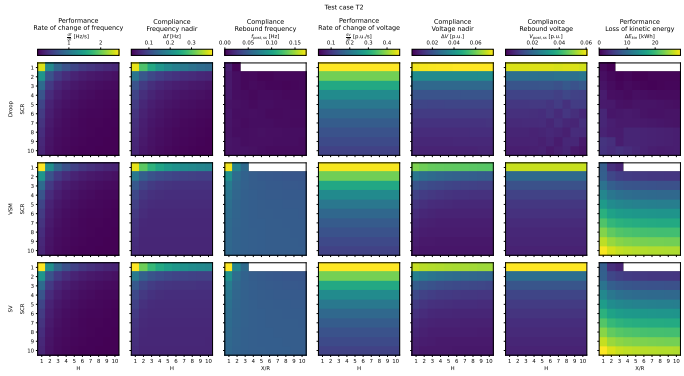

(**c**) Real values (Test #2)

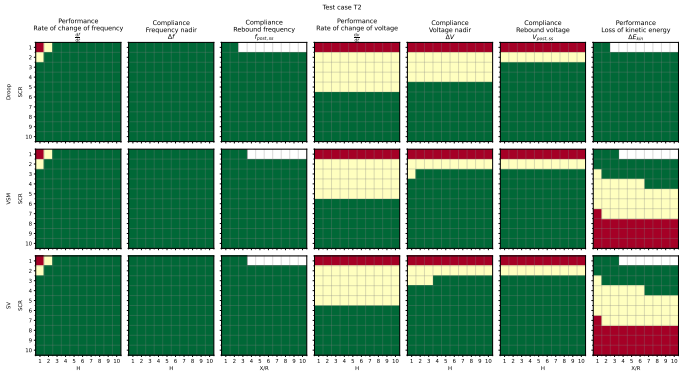

(**d**) Pass/fail mapping (Test #2)

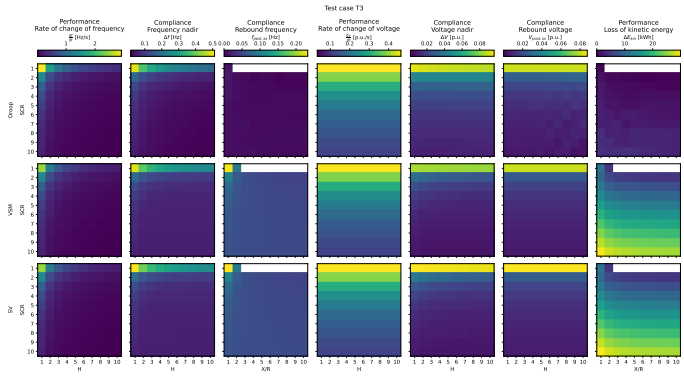

(**e**) Real values (Test #3)

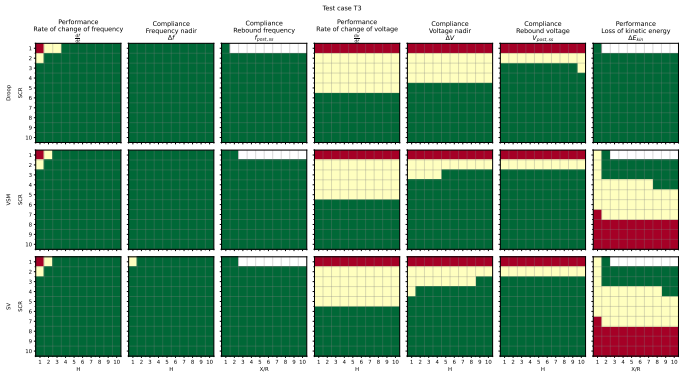

(**f**) Pass/fail mapping (Test #3)

**Figure 14.** Benchmark results.

General Remarks

The frequency compliance from the disturbances were very small and far from being uncompliant. However, these frequency disturbances challenged voltage compliance.

Lower $X/R$ ratios were shown to support transient voltage stability, but not with a great impact, and this is far from desired when considering the compliant solution space in Section 3. The note on the limited power transfer capabilities with low $X/R$ ratios in [20] and the increased resistance with increased losses did not further aid the imperative to strengthen the grid with lower $X/R$ ratios. Lower $X/R$ ratios also increased the frequency of the response, $\omega$, in the frequency stability plot (Figure 13c,e).

**Table 5.** Impacts of the compliance parameters.

| ***Benchmark Parameter*** | | | ***Impact Level*** [(b)] | | | ***Data Manipulation*** | |
|---|---|---|---|---|---|---|---|
| **Symbol** | **Unit** | **Type** [(a)] | **SCR** | **X/R** | **H** | **Dim.** [(c)] | **P < W < F** [(d)] |
| $\frac{df}{dt}$ | Hz/s | P | H | L | H | X/R | 0 < 1 < 2 |
| $\Delta f$ | Hz | C | H | L | H | X/R | 0 < 0.5 < 2 |
| $f_{post,ss}$ | Hz | C | L | M | - | H | 0 < 0.5 < 2 |
| $\frac{dv}{dt}$ | p.u./s | P | H | L | H | X/R | 0 < 0.2 < 0.4 |
| $\Delta v$ | p.u. | C | H | L | H | X/R | 0 < 0.02 < 0.05 |
| $v_{post,ss}$ | p.u. | C | H | L | - | X/R | 0 < 0.02 < 0.05 |
| $\Delta E_{kin}$ | kWh | P | L | M | - | H | 0 < 10 < 20 |

[(a)] P = Performance, C = Compliance, [(b)] H = High, M = Medium, L = Low, [(c)] Reduced dimension, [(d)] P = Pass, W = Warn, F = Fail.

### *6.3. Compliance Capabilities*

The compliance results are found in Figure 14 and are commented on in the following subsections.

#### 6.3.1. Frequency Parameters

Only the performance parameter for the ROCOF with thresholds defined by CIGRE's weak grid definition [3] "failed" for SCR = 1 and X/R = 1. This meant that the ROCOF could be classified as a very weak grid for disturbances of ±5% of the nominal power of the OWF.

This result was not different across the GFM controls and was almost completely the same across the tests. Only the droop control differed by not converging with any simulations in this grid condition. However, the droop control would fail every response in test case #1 anyway if a DC-link were implemented in the model. It is acknowledged in this study that it is essential to model the DC-link for frequency disturbances, as the stored energy in the DC-link is exploited during the emulation of inertia [57].

The compliance parameters regarding frequency passed every successive RMS simulation, regardless of the grid strength. This indicated that the GFM controls were compliant with the frequency requirements during frequency disturbances with power imbalances up to 5% of the OWF's available capacity.

It must be noted that the lack of DC-link modeling challenges this standpoint. It is, however, expected that the frequency will adjust accordingly for the VSM and SV until a sufficient current capacity is gained.

#### 6.3.2. Voltage Parameters

It is obvious from the figures of the pass/fail criteria that the biggest issue resulting from frequency disturbances is the voltage stability in weak grids. The SCR parameters are the dominant deciding factors for compliance issues. In particular, when SCR = 1, it is almost impossible for an OWF to counter the power imbalance and avoid classifications of system incidents, i.e., when the voltage diverges more than 5% from the nominal voltage.

The performance parameter was almost identical in its results across the tests and GFM controls. The more important compliance parameters, $\Delta V$ and $V_{post,ss}$, had some small differences. The VSM is the best-performing GFM control in weak grids, followed closely by the SV. The droop control consequently achieved warning flags from SCR $\leq$ 4.

#### 6.3.3. Energy Parameters

The kinetic energy lost due to the frequency deviations after a disturbance increased for a larger SCR and a lower X/R, and the SCR was the most dominant factor. The lost kinetic energy parameter indicated how much energy the grid had contributed in order to support the frequency stability.

## 7. Evaluation of Results

*Frequency and Voltage Stability (Benchmark Parameters)*

Regarding the frequency stability, no compliance issues were discovered across the various test cases, GFM controls, and SCR, X/R, and H values. The grid was only classified as weak or very weak when $SCR \leq 2$ and $X/R \leq 2$ while being subjected to a frequency disturbance equivalent to a power imbalance of $\pm$ 5 % $P_{OWF}$.

The following table summarizes the best GFM controls in the individual tests. The conclusions were drawn by counting the numbers of passed tests. Cells noted with a "-" indicate that the performance was identical and, thus, non-comparable. The GFM controls has the following abbreviations: droop control (D), virtual synchronous machine (VSM), and synchronverter (SV).

It is seen in Table 6 that the droop control is represented in five cells, the SV is represented in seven cells, and the VSM is represented in 11 cells. The VSM is, thus, the most compliant and reliable GFM control for weak grid conditions. The VSM is dominant in almost all benchmark parameters and shows supremacy in terms of the voltage nadir. This is a significant feature, as the voltage stability is a general issue for weak grids.

**Table 6.** Summary of the best-performing GFM controls with respect to the benchmark parameters.

| Test | $\frac{df}{dt}$ | $\Delta f$ | $f_{post,ss}$ | $\frac{dv}{dt}$ | $\Delta v$ | $v_{post,ss}$ | $E_{kin,loss}$ |
|---|---|---|---|---|---|---|---|
| **#1** | SV/VSM | - | SV/VSM | D | VSM | SV/VSM | D |
| **#2** | - | - | SV/VSM | - | VSM | - | D |
| **#3** | SV/VSM | D/VSM | SV/VSM | - | VSM | SV/VSM | D |

All GFM controls failed the performance test when SCR = 1. Recalling that the GFM control responds to the SCR at the terminals, it is acknowledged that the SCR demarcated for failing GFM controls might be even lower if the SCR is considered at the WT terminals and not at the POI.

## 8. Conclusions and Future Work

There is a need for a standardization of grid-strength classification that considers the inertia, and impedance magnitude, and angle at the connection point.

This was made clear in a sensitivity study of 9000 RMS simulations, where seven performance parameters were used to quantify the frequency and voltage compliance capabilities of GFM control strategies. The quantification resulted in VSM being the best GFM control and droop control being the worst with respect to frequency disturbances.

Future studies will concern the following: (***a***) the inclusion of DC-link modeling in GFM-controlled converters; (***b***) a continuation of the studies of GFM controls in weak grid conditions with EMT simulations for more precise and detailed results;(***c***) eigenvalue analyses of weak grid conditions with respect to the SCR, $X/R$, and inertia constant $H$; (***d***) studies of the role of GFM control in converter-based power generation at the distribution level in weak grid conditions.

**Author Contributions:** Conceptualization, B.V.; methodology, B.V., P.J.R., J.H. and H.J.; formal analysis, B.V., P.J.R., J.H. and H.J.; investigation, B.V.; writing—original draft preparation, B.V.; writing—review and editing, B.V., P.J.R., H.J.; J.H. and A.K.; visualization, B.V.; supervision, P.J.R., J.H. and H.J.; All authors have read and agreed to the published version of the manuscript.

**Funding:** This research received no external funding.

**Acknowledgments:** We would like to thank Oguzhan Ceylan, Murat Gol, and Aydogan Ozdemir for organizing the 57th Universities Power Engineering Conference (UPEC) at Istanbul Technical University. Your dedication to making this conference a success is greatly appreciated.

**Conflicts of Interest:** The authors declare no conflict of interest.

## Abbreviations

The following abbreviations are used in this manuscript:

| | |
|---|---|
| D | Droop control |
| GFL | Grid-following |
| GFM | Grid-forming |
| OWF | Offshore wind farm |
| OSS | Offshore substation |
| ONS | Onshore substation |
| PLL | Phase-locked loop |
| ROCOF | Rate of change of frequency |
| SCR | Short-circuit ratio |
| SG | Synchronous generator |
| SV | Synchronverter |
| VSM | Virtual synchronous machine |
| WT | Wind turbine |
| X/R | Reactance–resistance ratio |

## Subscripts

The following subscripts are used in this manuscript:

| | |
|---|---|
| $g$ | grid |
| $kin$ | Kinetic entity |
| $LN$ | Line |
| $LD$ | Load |
| $nom$ | Nominal entity |
| $rat$ | Rated entity |
| $r$ | Receiving end or rotor |
| $s$ | Sending end |
| $th$ | Thevenin equivalent |
| $tot$ | Total entity |

## Symbols

The following symbols are used in this manuscript:

| | |
|---|---|
| $\mathbf{X}$ | Matrix or vector formed of elements $x_i$ |
| $\Delta P$ | Power imbalance |
| $\delta, \theta$ | Angle |
| $\omega$ | Angular velocity |
| $\tau a$ | Acceleration time constant |
| $\mathcal{C}$ | Compliant solution space |
| $\mathcal{F}$ | Feasible solution space |
| $\mathcal{S}$ | Solution space |
| $E$ | Voltage or kinetic energy |
| $Ha$ | Inertia constant |
| $I$ | Current |
| $J$ | Moment of inertia |
| $m_x$ | Droop coefficient of $x$ |
| $P$ | Active power |
| $Q$ | Reactive power |
| $R$ | Resistance |
| $V$ | Voltage |
| $X$ | Reactance |
| $Z$ | Impedance |

## Appendix A. Grid-Forming Block Diagrams

All block diagrams are from PowerFactory 2021 SP4.

### *Appendix A.1. Droop Control*

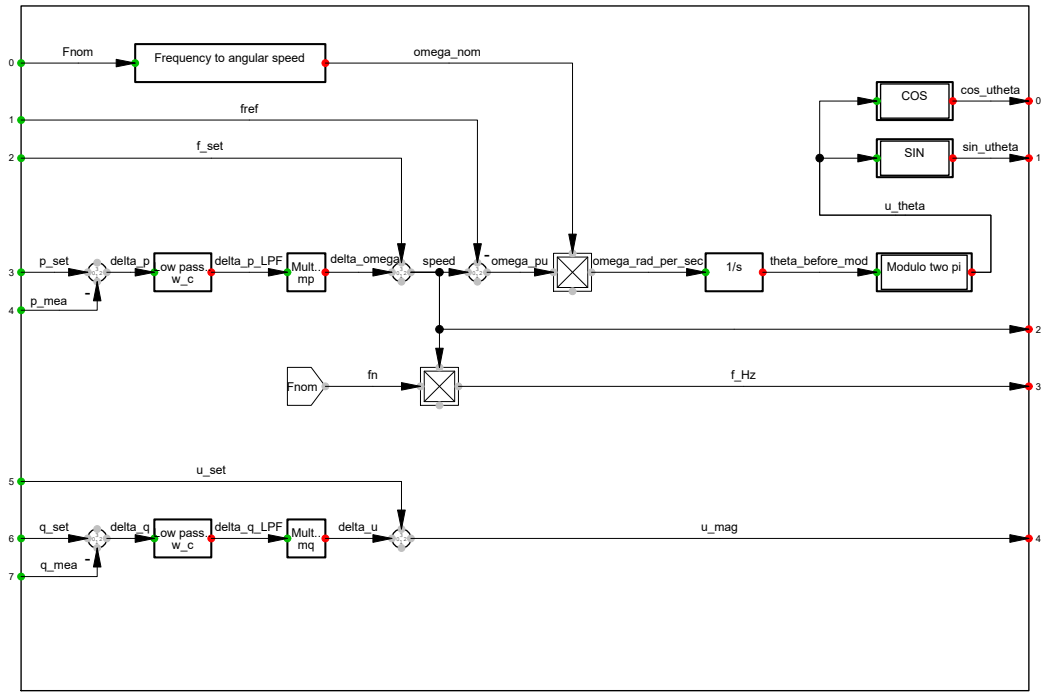


**Figure A1.** Droop control. See Section 4.1 for details.

### *Appendix A.2. Virtual Synchronous Machine*

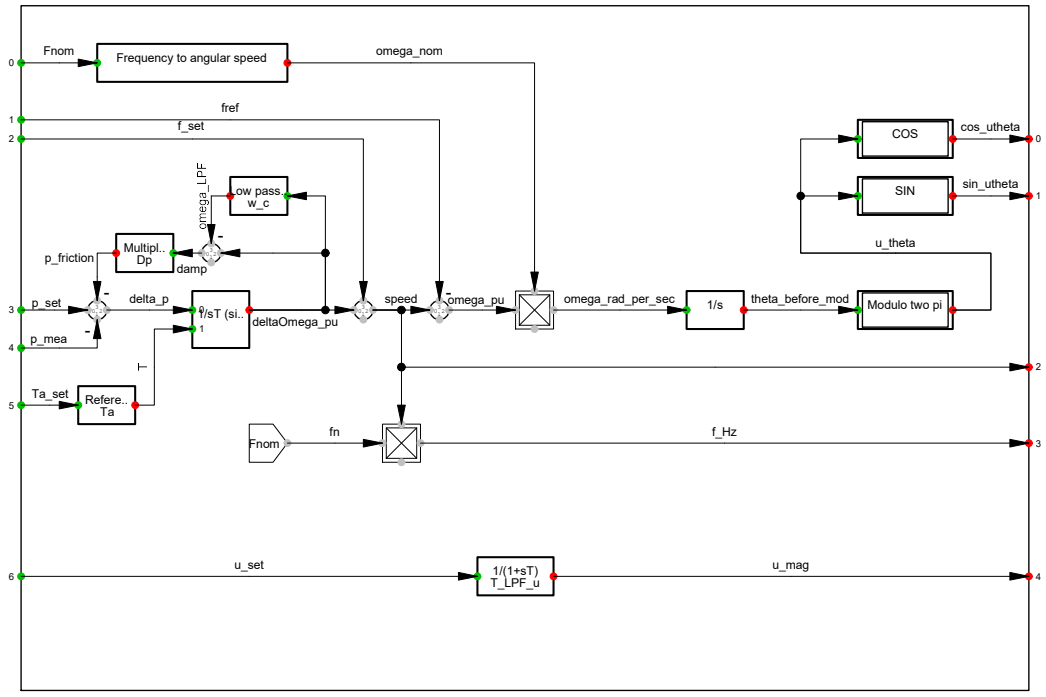


**Figure A2.** Virtual synchronous machine (VSM). See Section 4.2 for details.

*Appendix A.3. Synchronverter*

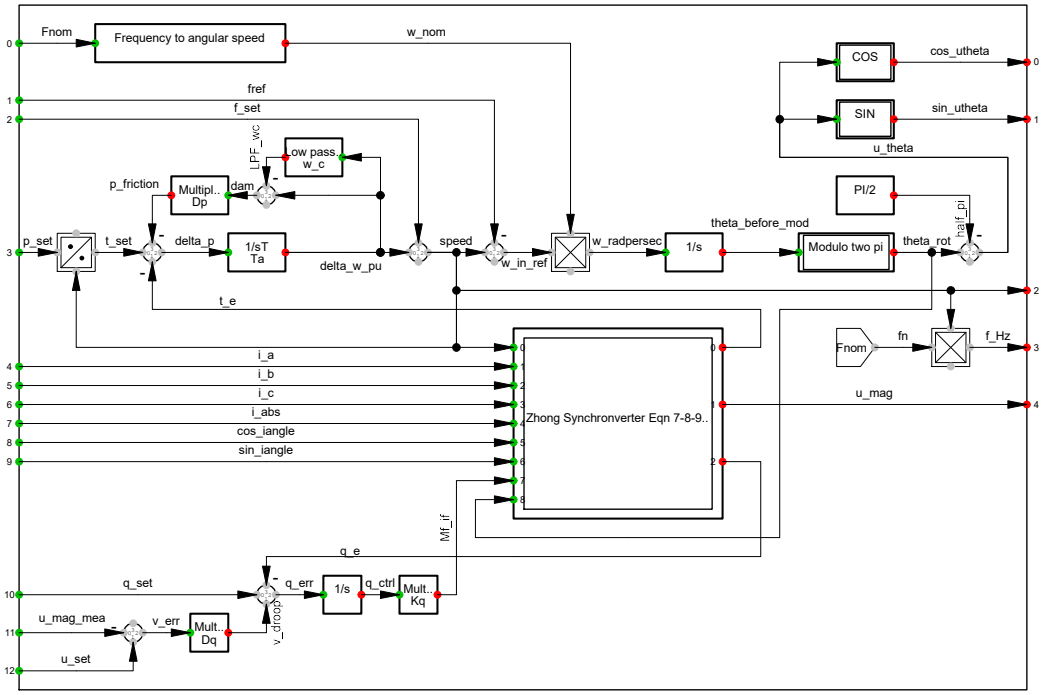


**Figure A3.** Synchronverter control. See Section 4.3 for details.

*Appendix A.4. Tuning Constants for the Grid-Forming Control System*

**Table A1.** The tuning constants implemented in the grid-forming control in the DSL modules from the PowerFactory templates.

| Block | Description | Variable | Value | Unit | D | SV | VSM |
|---|---|---|---|---|---|---|---|
| **Droop** | Active power droop coefficient | mp | 0.01 | [-] | ✓ | | |
| | Reactive power droop coefficient | mq | 0.05 | [-] | ✓ | | |
| | Low-pass filter cut-off frequency | w_c | 60 | [Hz] | ✓ | | |
| | initial speed setting | f_setpoint | 1 | [p.u.] | ✓ | | |
| **Synchronverter** | Acceleration time const. | Ta | 3 | [s] | | ✓ | |
| | Damping coefficient | Dp | 100 | [-] | | ✓ | |
| | Voltage gain | Kq | 1000 | [-] | | ✓ | |
| | Reactive power droop coefficient | Dq | 20 | [-] | | ✓ | |
| | Damping filter cut-off freq. | w_c | 0 | [rad/s] | | ✓ | |
| | Initial speed setting | f_setpoint | 1 | [p.u.] | | ✓ | |
| **VSM** | Acceleration time constant | Ta | 3 | [s] | | | ✓ |
| | Damping coefficient | Dp | 100 | [-] | | | ✓ |
| | Damping filter cut-off frequency | w_c | 0 | [rad/s] | | | ✓ |
| | Voltage setpoint low-pass filter time constant | T_LPF_u | 0.003 | [s] | | | ✓ |
| | Initial speed setting | f_setpoint | 1 | [p.u.] | | | ✓ |
| **Virtual impedance** | Basic virtual resistance | r | 0.006 | [p.u.] | ✓ | ✓ | ✓ |
| | Basic virtual reactance | x | 0.006 | [p.u.] | ✓ | ✓ | ✓ |
| | Control mode: 0 = const. Z; 1 = Proportional over-current limitation | Mode | 1 | | ✓ | ✓ | ✓ |
| | Over-current threshold | i_lim | 1.01 | [p.u.] | ✓ | ✓ | ✓ |
| | Proportional factor for additional r | kpr | 8 | [-] | ✓ | ✓ | ✓ |
| | Proportional factor for additional x | kpx | 8 | [-] | ✓ | ✓ | ✓ |
| | Time constant of low-pass filter | T_lpf | 0.0001 | [s] | ✓ | ✓ | ✓ |

**Table A1.** *Cont.*

| Block | Description | Variable | Value | Unit | D | SV | VSM |
|---|---|---|---|---|---|---|---|
| **Output voltage** | Current limitation: 0 = disabled; 1 = enabled | Mode | 1 | | ✓ | ✓ | ✓ |
| | Maximum current | i_max | 1.2 | [p.u.] | ✓ | ✓ | ✓ |
| | Series resistance | Rseries | 0 | [%] | ✓ | ✓ | ✓ |
| | Series reactance | Xseries | 10 | [%] | ✓ | ✓ | ✓ |
| **Voltage control** | Measurement filter time constant | Tr | 0.02 | [s] | | | ✓ |
| | Controller gain | K | 0.5 | [-] | | | ✓ |
| | Minimum AVR output voltage | u_set_min | -1.5 | [p.u.] | | | ✓ |
| | Maximum AVR output voltage | u_set_max | 1.5 | [p.u.] | | | ✓ |

## References


1. Milborrow, D. Wind Energy Development. In *The Age of Wind Energy*; Springer: Cham, Switzerland, 2019; pp. 3–22. [CrossRef]
2. Koutiva, X.I.; Vrionis, T.D.; Vovos, N.A.; Giannakopoulos, G.B. Optimal integration of an offshore wind farm to a weak AC grid. *IEEE Trans. Power Deliv.* **2006**, *21*, 987–994. [CrossRef]
3. CIGRE. *Connection of Wind Farms to Weak AC Networks*; Technical Report No. B4.62; (Reference 671); CIGRE: Paris, France, 2016.
4. Abreu, L.V.; Shahidehpour, M. Wind energy and power system inertia. In Proceedings of the 2006 IEEE Power Engineering Society General Meeting, Montreal, QC, Canada, 18–22 June 2006; p. 1709240. [CrossRef]
5. Vilmann, B.; Hjerrild, J.; Randewijk, P.J.; Khalil, A. Frequency and Voltage Compliance Capability of Grid-Forming Wind Turbines in Offshore Wind Farms in Weak Grids with a Power Imbalance. In Proceedings of the 2022 57th International Universities Power Engineering Conference (UPEC), Istanbul, Turkey, 30 August–2 September 2022; p. 8. [CrossRef]
6. Bindner, H. *Power Control for Wind Turbines in Weak Grids: Concepts Development*; Forskningscenter Risø: Roskilde. Denmark, 1999; p. 40.
7. NERC. *Integrating Inverter-Based Resources into Low Short Circuit Strength Systems—Reliability Guideline*; NERC: Washington, DC, USA, 2017.
8. Sepehr, A.; Gomis-Bellmunt, O.; Pouresmaeil, E. Employing Machine Learning for Enhancing Transient Stability of Power Synchronization Control During Fault Conditions in Weak Grids. *IEEE Trans. Smart Grid* **2022**, *13*, 2121–2131. [CrossRef]
9. Lorenzen, S.L.; Nielsen, A.B.; Bede, L. Control of a grid connected converter during weak grid conditions. In Proceedings of the 2016 IEEE 7th International Symposium on Power Electronics for Distributed Generation Systems, PEDG, Vancouver, BC, Canada, 27–30 June 2016. [CrossRef]
10. *IEC 60909-0:2016*; Short-Circuit Currents in Three-Phase a.c. Systems—Part 0: Calculation of Currents. International Electrotechnical Commission: Geneva, Switzerland, 2016.
11. Berhausen, S.; Boboń, A. Determination of high power synchronous generator subtransient reactances based on the waveforms for a steady state two-phase short-circuit. *Appl. Math. Comput.* **2018**, *319*, 538–550. [CrossRef]
12. *IEEE 1110-2019*; Guide for Synchronous Generator Modeling Practices and Parameter Verification with Applications in Power System Stability Analyses. IEEE: Piscataway, NJ, USA, 2020.
13. CIGRE. *Guide for Planning DC Links Terminating at AC Systems Locations Having Low Short-Circuit Capacities (Part I: AC/DC Interaction Phenomena)*; Technical Report No. 14.07; (AC/DC System Interaction), IEEE Working Group 15.05.05 (HVDC Interaction with low SCR AC Systems); CIGRE Working Group: Paris, France, 1992.
14. Etxegarai, A.; Eguia, P.; Torres, E.; Fernandez, E. Impact of wind power in isolated power systems. In Proceedings of the Mediterranean Electrotechnical Conference—MELECON, Yasmine Hammamet, Tunisia, 25–28 March 2012; pp. 63–66. [CrossRef]
15. Fu, R.; Li, L.; Wang, X.; Lv, X. Critical SCR for the stability of VSC connected to weak grid. In Proceedings of the IEEE Power and Energy Society General Meeting, Montreal, QC, Canada, 02–06 August 2020. [CrossRef]
16. Chawda, G.S.; Shaik, A.G. Power Quality Mitigation in Weak AC Grid with Low X/R Ratios using Distribution Static Compensator Controlled by LMF Algorithm. In Proceedings of the 2020 IEEE Region 10 Symposium, TENSYMP, Dhaka, Bangladesh, 5–7 June 2020; pp. 44–47. [CrossRef]
17. Dozein, M.G.; Mancarella, P.; Saha, T.K.; Yan, R. System strength and weak grids: Fundamentals, challenges, and mitigation strategies. In Proceedings of the Australasian Universities Power Engineering Conference, Aupec, Auckland, New Zealand, 27–30 November 2018; p. 8757997. [CrossRef]
18. Boričić, A.; Torres, J.L.R.; Popov, M. System Strength: Classification, Evaluation Methods, and Emerging Challenges in IBR-dominated Grids. In Proceedings of the 11th International Conference on Innovative Smart Grid Technologies—Asia, ISGT-Asia 2022, Singapore, Singapore, 1–5 November 2022; pp. 185–189. [CrossRef]
19. Kumkratug, P. The effect of R/X ratio of the short transmission line on transient stability. *Am. J. Appl. Sci.* **2012**, *9*, 365–367. [CrossRef]
20. Huang, L.; Wu, C.; Zhou, D.; Blaabjerg, F. Grid Impedance Impact on the Maximum Power Transfer Capability of Grid-Connected Inverter. In Proceedings of the Energy Conversion Congress and Exposition—Asia, ECCE Asia, Singapore, Singapore, 24–27 May 2021; pp. 1487–1490. [CrossRef]

21. Ebrahimzadeh, E.; Blaabjerg, F.; Lund, T.; Nielsen, J.G.; Kjær, P.C. Modelling and stability analysis of wind power plants connected to weak grids. *Appl. Sci.* **2019**, *9*, 4695. [CrossRef]
22. Devadason, J.; Moses, P.S.; Masoum, M.A. Stability domain analysis and enhancement of squirrel cage induction generator wind turbines in weak grids. *Energies* **2021**, *14*, 4786. [CrossRef]
23. Lund, T.; Wu, H.; Soltani, H.; Nielsen, J.G.; Andersen, G.K.; Wang, X. Operating Wind Power Plants under Weak Grid Conditions Considering Voltage Stability Constraints. *IEEE Trans. Power Electron.* **2022**, *37*, 15482–15492. [CrossRef]
24. Li, Y.; Chen, J.; Wang, X.; Zhang, X.; Zhao, X. Dynamic Stability Study of Grid-Connected Inverter Based on Virtual Synchronizer under Weak Grid. *Energies* **2022**, *15*, 7091. [CrossRef]
25. Gonzalez-Longatt, F.M. Impact of emulated inertia from wind power on under-frequency protection schemes of future power systems. *J. Mod. Power Syst. Clean Energy* **2016**, *4*, 211–218. [CrossRef]
26. Energinet. *Teknisk Forskrift 3.2.5 for Vindkraftanlæg Større End 11 kW*; Energinet: Fredericia, Denmark, 2016.
27. National Grid House. *System Operability Framework*; National Grid House: Warwick, UK, 2016.
28. ESO, N.G. Technical Report on the Events of 9 August 2019. 2019. Available online: https://www.nationalgrideso.com/document/152346/download (accessed on 30 January 2023).
29. ENTSOE. *Continental Europe Synchronous Area Separation on 8 January 2021*; ACER: Ljubljana, Slovenia, 2021.
30. Ippolito, M.G.; Musca, R.; Zizzo, G. Analysis and simulations of the primary frequency control during a system split in continental europe power system. *Energies* **2021**, *14*, 1456. [CrossRef]
31. Rosso, R.; Wang, X.; Liserre, M.; Lu, X.; Engelken, S. Grid-Forming Converters: Control Approaches, Grid-Synchronization, and Future Trends—A Review. *IEEE Open J. Ind. Appl.* **2021**, *2*, 93–109. [CrossRef]
32. Zhang, X.; Xia, D.; Fu, Z.; Wang, G.; Xu, D. An Improved Feedforward Control Method Considering PLL Dynamics to Improve Weak Grid Stability of Grid-Connected Inverters. *IEEE Trans. Ind. Appl.* **2018**, *54*, 5143–5151. [CrossRef]
33. Lu, L. *Enhanced Frequency Control Capability from Wind Turbines and Farms*; DTU Wind Energy: Roskilde, Denmark, 2022. [CrossRef]
34. Fan, L. Modeling Type-4 Wind in Weak Grids. *IEEE Trans. Sustain. Energy* **2019**, *10*, 8392724. [CrossRef]
35. Li, Y.; Meng, K.; Dong, Z.Y. Converter-driven voltage instability in weak grid considering cross-domain impedance. *IEEE Power Energy Soc. Gen. Meet.* **2020**, *2020*, 9282051. [CrossRef]
36. Li, Y.; Yuan, X.; Li, J.; Xiao, H.; Xu, Z.; Du, Z. Novel grid-forming control of PMSG-based wind turbine for integrating weak AC grid without sacrificing maximum power point tracking. *Iet Gener. Transm. Distrib.* **2021**, *15*, 1613–1625. [CrossRef]
37. Hesse, R.; Turschner, D.; Beck, H.P. Micro grid stabilization using the virtual synchronous machine (VISMA). *Renew. Energy Power Qual. J.* **2009**, *1*, 472. [CrossRef]
38. Chen, Y.; Hesse, R.; Turschner, D.; Beck, H.P. Dynamic properties of the virtual synchronous machine (VISMA). *Renew. Energy Power Qual. J.* **2011**, *1*, 755–759. [CrossRef]
39. Zhong, Q.C.; Weiss, G. Synchronverters: Inverters that mimic synchronous generators. *IEEE Trans. Ind. Electron.* **2011**, *58*, 1259–1267. [CrossRef]
40. Pagnani, D.; Blaabjerg, F.; Bak, C.L.; Silva, F.M.F.d.; Kocewiak, L.; Hjerrild, J. Offshore Wind Farm Black Start Service Integration: Review and Outlook of Ongoing Research. *Energies* **2020**, *13*, 6286. [CrossRef]
41. Kong, L.; Xue, Y.; Qiao, L.; Wang, F.F. Angle Droop Design for Grid-Forming Inverters Considering Impacts of Virtual Impedance Control. In Proceedings of the 2021 IEEE Energy Conversion Congress and Exposition, ECCE 2021-Proceedings, Vancouver, BC, Canada, 10–14 October 2021; pp. 1006–1013. [CrossRef]
42. Beck, H.P.; Hesse, R. Virtual synchronous machine. In Proceedings of the 2007 9th International Conference on Electrical Power Quality and Utilisation, EPQU, Barcelona, Spain, 9–11 October 2007. [CrossRef]
43. D'Arco, S.; Suul, J.A. Virtual synchronous machines - Classification of implementations and analysis of equivalence to droop controllers for microgrids. In Proceedings of the 2013 IEEE Grenoble Conference PowerTech, POWERTECH, Grenoble, France, 16–20 June 2013. [CrossRef]
44. Musca, R.; Vasile, A.; Zizzo, G. Grid-forming converters. A critical review of pilot projects and demonstrators. *Renew. Sustain. Energy Rev.* **2022**, *165*, 112551. [CrossRef]
45. National Grid. *National Grid, GC0137: Minimum Specification Required for Provision of GB Grid Forming (GBGF) Capability (Formerly Virtual Synchronous Machine/VSM Capability)*; National Grid: London, UK, 2022.
46. Wall, P.; Gonzalez-Longatt, F.; Terzija, V. Demonstration of an inertia constant estimation method through simulation. In Proceedings of the 2010 45th International Universities Power Engineering Conference (UPEC 2010), Cardiff, UK, 31 August–3 September 2010; IEEE: Piscataway, NJ, USA, 2010.
47. Huang, L.; Wu, C.; Zhou, D.; Blaabjerg, F. Impact of Grid Strength and Impedance Characteristics on the Maximum Power Transfer Capability of Grid-Connected Inverters. *Appl. Sci.* **2021**, *11*, 4288. [CrossRef]
48. Jóhannsson, H. Development of Early Warning Methods for Electric Power Systems. Ph.D. Thesis, Technical University of Denmark, Lyngby, Denmark, 2011.
49. Kundur, P.S. *Power system Stability and Control*; Mc Graw Hill Education (India) Private Limited: Uttar Pradesh, India, 1994; p. 1176.
50. Johnson, M.; Vaziri, M.; Vadhva, S. Understanding slow voltage instability. In Proceedings of the 2012 Ieee 13th International Conference on Information Reuse and Integration, Iri 2012, Las Vegas, NV, USA, 8–10 August 2012; pp. 502–508. [CrossRef]
51. Concordia, C. Voltage instability. *Int. J. Electr. Power Energy Syst.* **1991**, *13*, 14–20. [CrossRef]

52. Dorile, P.O.; Jagessar, D.R.; McCann, R.A. Techno-economic assessment of voltage stability improvement using SSSC and STATCOM in a wind-dominated power system. In Proceedings of the 2021 IEEE Kansas Power and Energy Conference, Kpec 2021, Manhattan, KS, USA, 19–20 April 2021; p. 6. [CrossRef]
53. Rocabert, J.; Luna, A.; Blaabjerg, F.; Rodríguez, P. Control of power converters in AC microgrids. *IEEE Trans. Power Electron.* **2012**, *27*, 6200347. [CrossRef]
54. Hansen, J.B.; Osterfelt, S.T.; Randewijk, P.J. The use of synchronverters for fast frequency response and automatic voltage regulation in low inertia islanded power networks. In Proceedings of the 2021 56th International Universities Power Engineering Conference: Powering Net Zero Emissions, UPEC 2021-Proceedings, Middlesbrough, UK, 31 August–3 September 2021. [CrossRef]
55. *Guidance Notes for Power Park Modules, EU Code Users—Issue 3*; Technical Report No.; National Grid ESO: Warwick, UK, 2021.
56. Reddy, P.B.; Hiskens, I.A. Limit-induced stable limit cycles in power systems. In Proceedings of the 2005 IEEE Russia Power Tech, PowerTech, St. Petersburg, Russia, 27–30 June 2005. [CrossRef]
57. Berizzi, A.; Bosisio, A.; Ilea, V.; Marchesini, D.; Perini, R.; Vicario, A. Analysis of Synthetic Inertia Strategies from Wind Turbines for Large System Stability. *IEEE Trans. Ind. Appl.* **2022**, *58*, 3184–3192. [CrossRef]